Effect of Magnetic Resonance Imaging on the Motion Accuracy of Magnetic Resonance Imaging-compatible Focused Ultrasound Robotic System

Anastasia Antoniou, Nikolas Evripidou, Antreas Chrysanthou[1], Leonidas Georgiou[1], Cleanthis Ioannides[1], Kyriakos Spanoudes[2], Christakis Damianou

Department of Electrical Engineering, Computer Engineering, and Informatics, Cyprus University of Technology, [1]Department of Interventional Radiology, German Oncology Center, Limassol, [2]VET EX MACHINA Limited, Nicosia, Cyprus

Abstract

Purpose: The current study provides insights into the challenges of safely operating a magnetic resonance imaging (MRI)-guided focused ultrasound (MRgFUS) robotic system in a high-field MRI scanner in terms of robotic motion accuracy. **Materials and Methods:** Grid sonications were carried out in phantoms and excised porcine tissue in a 3T MRI scanner using an existing MRgFUS robotic system. Fast low-angle shot-based magnetic resonance thermometry was employed for the intraprocedural monitoring of thermal distribution. **Results:** Strong shifting of the heated spots from the intended points was observed owing to electromagnetic interference (EMI)-induced malfunctions in system's operation. Increasing the slice thickness of the thermometry sequence to at least 8 mm was proven an efficient method for preserving the robotic motion accuracy. **Conclusions:** These findings raise awareness about EMI effects on the motion accuracy of MRgFUS robotic devices and how they can be mitigated by employing suitable thermometry parameters.

Keywords: Compatibility, focused ultrasound, motion accuracy, magnetic resonance thermometry, robotic system, slice thickness

INTRODUCTION

Magnetic resonance imaging (MRI) offers several advantages compared to other medical imaging modalities, including its nonionizing nature and excellent contrast resolution for soft tissues, and it is widely employed for the intraprocedural guidance of therapeutic interventions.[1] MRI-compatible robotics has emerged as a useful tool for enhancing MRI-guided interventional procedures by facilitating the precise positioning and manipulation of surgical instruments and energy sources, thus enabling safer and more effective patient treatment.[2] Nevertheless, there exist numerous challenges in the wider adaption of MRI-guided robotic-assisted applications, mainly arising from the strong static magnetic field, rapidly switching magnetic field gradients, and radiofrequency (RF) pulses, as well as the susceptibility to electrical noise and confined space of the MRI scanner.[1]

The design of robotic systems for operation inside high-field MRI scanners is complicated by the limitations of using conventional construction materials, sensors, and actuators since they constitute the primary sources of electromagnetic interference (EMI) with the scanner. The strong static field can exert rotational or translation forces on ferrous components, whereas nonferromagnetic electronics, such as motion actuators and sensors, might produce electric currents when exposed to the gradient and RF fields.[3,4] In general, ensuring MRI compatibility of mechatronic devices involves meeting three key requirements: (1) maintaining magnetic resonance (MR) safety, (2) preserving image quality, and (3) operating properly without any EMI-induced malfunctions.[4]

Typically, when evaluating the MRI compatibility of motion actuators and controllers, the focus is placed on assessing the

Address for correspondence: Prof. Christakis Damianou, Department of Electrical Engineering, Computer Engineering and Informatics, Cyprus University of Technology, 30, Archbishop Kyprianou Street, Limassol 3036, Cyprus.
E-mail: christakis.damianou@cut.ac.cy

Access this article online

Quick Response Code:

Website:
www.jmp.org.in

DOI:
10.4103/jmp.jmp_7_24

impact of their activation on the generated images in terms of introduced artifacts and the signal-to-noise ratio (SNR).[5-11] The degree of impact on the imaging quality varies based on the chosen imaging sequence and coil.[12,13] In general, if the image quality remains satisfactory, most studies conclude that the tested mechatronic component is MRI-compatible. However, what is often overlooked is how these components are directly affected in the MRI environment in terms of their own functionality.

Although optical encoders are extensively employed for detecting the position of rotary and linear stages in the MRI, their electrical pulses can result in considerable noise emission.[4,14] Electrical motion sensors can not only introduce noise into the imaging process but also receive signals from the RF pulses, which may negatively affect their operation depending on their proximity to the RF coil.[4] So far, the encoders' operation has been predominantly assessed by monitoring the encoder counts during imaging.[13,15,16] In their study, Goldenberg *et al.*[13] drew attention to the issue of EMI-induced abnormal signal counting by motion sensors during the performance evaluation of a robotic system for MRI-guided prostatic interventions in a 1.5 T MRI scanner. Specifically, the optical encoders incorrectly interpreted EMI noise as motion signals, thus resulting in the motion controller receiving inaccurate position information from the counter. The authors proposed as a solution to preserve the joint position data before scanning, ensure no motor motion during the scanning process, and subsequently restore the saved data.[13]

Knull *et al.*[15] also reported on errors in the encoder's counting of a piezoelectrically actuated system for automated needle placement to localized prostate cancer. In this study, the motion of the end effector was controlled by optical encoders generating square wave signals with frequency components capable of interfering with the RF signals of the scanner. As a result, despite the use of shielded cables, EMI manifested as sporadic increments or decrements in the encoder counts during pulse sequences, which reached several hundred counts per acquisition. Saving of preimaging encoder counts and restoring them if any malfunction occurs, as well as deactivating the encoder feedback during image acquisition, were proposed by authors as potential remedial measures. In another study,[16] the performance of a master-slave surgical system for MRI-guided breast biopsy was evaluated. It was reported that field inhomogeneities at the periphery of the test phantom reached up to 40 ppm, which according to the authors could introduce errors exceeding 5 mm in the tracking sensors. Other studies concluded no significant EMI interference of standard optical encoders with high-field MRI scanners (3T) since no miscounts were identified in the encoders during imaging.[17-20]

Traditional EMI mitigation methods, like the common mode noise rejection, seem to be ineffective in addressing the MRI compatibility issues of motion-sensing electronics.[4] Some studies have underlined the need to pause the operation of motors[21] and block the encoder signal[12,13] during the RF pulses to avoid EMI-induced failures in their operation. It is also advisable to physically isolate any electrical sensors and their wiring from the RF coil to minimize interference.[4,12] In addition, proper filtering, shielding, and grounding should be used in all wiring, and the power electronics should be hosted in EMI-shielded enclosures in case they will be placed in the operating room.[4,15] A different approach used by Chopra *et al.*[22] is to design the motors and encoders to operate below a threshold frequency in order to prevent interference near the resonant frequency of the MRI scanner.

The potential impact of MRI on the performance of sensing electronics in the framework of MR-guided therapeutic interventions has not been given the required consideration. EMI-induced encoder miscounting and wrong position estimates can lead to significant positioning errors and arbitrary mobility of surgical instruments and therapeutic sources, thus compromising the safety of the procedure.

MRI-guided focused ultrasound (MRgFUS) constitutes a continuously emerging technology for noninvasive oncological applications, with numerous robotic devices being developed.[23-30] Highly accurate robotic motion is required for delivering ultrasound energy with mm-level precision and achieving thermal ablation of specific tissue regions in a safe and efficient manner. Therefore, it is crucial to ensure that the MRI does not generate excessive interference to the motion electronics that could compromise the reliability of the encoded position and motion accuracy of the positioning mechanism. In this context, the current study reports the key outcomes of the performance evaluation of an existing MRgFUS preclinical robotic system[28] in a 3T MRI scanner, where MR thermometry-guided grid sonications were carried out in tissue-mimicking phantoms (TMPs) and freshly excised tissue. Systematic positioning errors of the ultrasonic source leading to off-target ultrasonic delivery and shifting of thermal lesions were identified and investigated by changing the fast low-angle shot (FLASH) sequence parameters. To the best of our knowledge, this study is the first to document the impact of EMI from a high-field MRI scanner on the performance of an MRgFUS robotic device in terms of motion accuracy and how this can be mitigated by employing suitable parameters for intraprocedural imaging.

MATERIALS AND METHODS

Magnetic resonance imaging-compatible focused ultrasound robotic system

Positioning device

An existing MRI-compatible robotic device incorporating a single element spherically focused ultrasonic transducer (frequency = 2.6 MHz; diameter = 50 mm; radius of curvature = 65 mm; efficiency = 30%, Piezo Hannas, Wuhan, China) was employed in the study. The device has a simple design with two main enclosures separating the mechatronic components from the ultrasonic source,[28] as shown in Figure 1a. The positioning mechanism enables
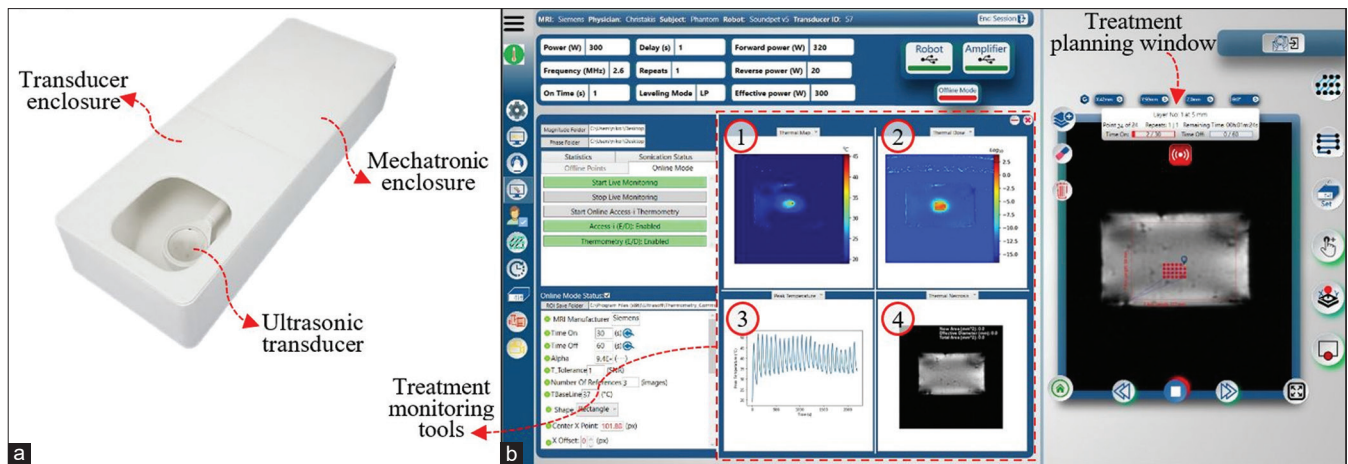
Figure 1: (a) Photo of the magnetic resonance imaging-guided focused ultrasound robotic device, (b) Screenshot of the main software window during grid sonication in a tissue-mimicking phantom with the treatment monitoring tools activated: (1) Temperature map, (2) Thermal dose map, (3) Time series of focal temperature evolution at the various sonication spots, and (4) Necrosis map overlaid on fast low-angle shot magnitude image of subject

motion of the ultrasonic source in three linear and one angular degrees of freedom using piezoelectric actuators (USR30-S3, Shinsei Kogyo Corp., Tokyo, Japan) while motion feedback is provided by optical encoders (EM10-500-I, US Digital Corporation, Vancouver, WA 98684, USA). The enclosure housing the transducer features a top acoustic opening that is sealed with a thin silicone membrane for placing the tissue of interest above the transducer's workspace. The device was designed with a compact size and manufactured with nonferrous materials to ensure compatibility with all conventional MRI scanners. The driving electronics of the device, i.e. motor drivers, microcontroller card, and DC supply, are enclosed within a single custom-made enclosure. The transducer is activated by an RF amplifier (AG1016, AG Series Amplifier, T and C Power Conversion, Inc., Rochester, USA). At this point, it should be noted that both the positioning mechanism and ultrasonic system underwent prior MRI compatibility assessments.[12] To enhance the SNR and image quality in the presence and operation of the system within the MRI bore, various setup parameters, such as the coil and target stability, and electronic components' placement relative to the imaging coil were tested and optimized. The outcomes demonstrated that the system can safely operate within high-field MRI scanners without experiencing operational malfunctions or introducing significant susceptibility artifacts that could comprise the acquired data while also maintaining adequate SNR for high-resolution imaging.

Treatment monitoring software

The accompanied therapy software enables efficient communication of the robotic device with the various peripheral devices, including the MRI scanner, driving system, and amplifier. The MRgFUS software can be interfaced with a 3T Magnetom Vida scanner (Siemens Healthineers, Erlangen, Germany) through the access-i software of Siemens, establishing both a passive link with the scanner for the dynamic transfer and processing of acquired images and an interactive link for full remote control of the scanner.

The treatment planning process begins by accessing the home menu and executing the robot's registration procedure based on a single Digital Imaging and Communications in Medicine (DICOM) image displaying the ultrasonic transducer, as positioned at the robot's coordinate origin. Initially, the software creates a yellow circle that matches the transducer's size. The user needs to accurately align this circle with the transducer's active element. This action, in turn, creates a marker at the center of the element, which is visible on the preoperative DICOM images used for treatment planning, thus precisely indicating the transducer's location within the treatment area. This streamlined digital registration process of the transducer within the area of interest on a single reference MRI image is considered advantageous as it eliminates the need for fiducial markers.

Regarding treatment planning, the user is allowed to draw the desired ablation pattern on preoperative MR images by either manually distributing random sonication points or determining a rectangular grid pattern of specific spatial resolution or selecting a nonuniform area, which is automatically covered by sonication points spaced by the selected step. These points are visited according to the sorting type (sequential, spiral, or zig-zag) defined by the user. Following the selection of the grid parameters (grid size, spatial, and temporal step), the user defines the ultrasonic parameters, i.e. the electric power to be applied to each point and the sonication duration.

The software further integrates a combination of therapy monitoring tools for the simultaneous display and dynamic update of temperature, thermal dose, and necrosis map, as well as a time series graph of the temperature evolution. Figure 1b is a screenshot of the main software window showing the aforementioned thermal monitoring tools.

Magnetic resonance-guided focused ultrasound heating of tissue-mimicking phantoms and *ex vivo* porcine tissue in grid patterns

In the framework of evaluating the performance of the employed robotic system in providing an efficient procedural workflow for MRgFUS interventions, multiple grid sonications were executed in agar-based TMPs and freshly excised porcine tissue. A mixture containing 6% weight per volume (w/v) agar (Merck KGaA, EMD Millipore Corporation, Darmstadt, Germany) and 4% w/v silicon dioxide (Sigma-Aldrich, St. Louis, Missouri, United States) dissolved in degassed, deionized water was prepared and let to solidify within a dedicated mold to form a rectangular phantom of 1980 cm³ volume. The preparation details of the phantom can be found in the article by Drakos *et al.*[31] This phantom type was found to possess an ultrasonic attenuation coefficient comparable to human soft tissue of 1.10 ± 0.09 dB/cm-MHz,[32] simultaneously offering realistic contrast in MRI.[33] The temperature and thermal dose distribution during heating within the agar phantom/porcine tissue (with a 60-s cooling period between successive sonications) was monitored by MR thermometry.

Experimental setup arrangement in the magnetic resonance imaging scanner

The experimental setup was arranged on the table of the 3T Siemens MRI scanner, as shown in Figure 2. The device was placed on the MRI table and the TMP/piece of porcine meat was securely positioned on the top of the membrane covering the acoustic opening. The imaging coil (body 18, Siemens Healthineers) was fixed a few cm above the phantom/meat using a custom-made plastic structure. The distance between the transducer and bottom surface of the subject was 35 mm, corresponding to a focal depth of 30 mm. Note that the mechatronic components were intentionally positioned outside of and as further away as possible from the coil detection region in order to reduce the possibility of EMI with the RF coil.[12]

The electronics' enclosure remained outside of the operating room and was connected to the device through EMI-shielded cables. Specifically, rubber-shielded copper cables (Shinsei Kogyo Corp., Tokyo, Japan) and a copper-shielded coaxial cable (RJ58, 50X) supplied the motors and transducer, respectively. In addition, a specially designed low-pass RF filter (10 MHz cutoff frequency, Anatech Electronics, Garfield, New Jersey, USA) was integrated between the transducer and the amplifier (T and C Power Conversion, Inc.) to suppress any harmonic currents.

Magnetic resonance thermometry monitoring of heating

Temperature maps were generated using the proton resonance frequency shift (PRFS) method.[34] This method exploits the temperature-dependent properties of hydrogen protons in tissue and is widely used in both the preclinical and clinical settings for monitoring thermal therapies. Initially, a baseline phase image was acquired at a known reference temperature (19°C). Then, during the heating and cooling periods, phase images were acquired at a temporal step of about 3s. The calculated phase changes among images were converted into temperature changes using the common PRFS thermometry equation as described by Rieke and Pauly.[34] The PRF coefficient was set at 0.0094 ppm/°C based on prior literature.[35-39]

Accumulation of a thermal dose equal to or higher than 240 CEM43°C (i.e., tissue exposed to a cumulative equivalent of 240 min at 43°C) was deemed as a successful necrosis of the exposed region.[40,41] The thermal dose calculation was automatically performed by the software according to equation 1:[42]

$$CEM\,43°C = \sum_{t=0}^{t=final} R^{(43-T)} \Delta t \qquad [1]$$

which correlates the cumulative number of equivalent minutes at 43°C (*CEM* 43°C) with the average temperature within the elapsed time Δt (*T*) and the rate of cell death (*R*), which equals to 0.25 when temperatures are smaller than 43°C and 0.5 otherwise. The thermal dose estimates were color-coded in a blue-to-red gradient, providing real-time information about the thermal dose distribution within the imaged region.

Temperature and thermal dose maps were extracted on a pixel-by-pixel basis via 2D FLASH coronal imaging with the body coil, with repetition time = 25 ms, echo time = 10 ms, flip angle = 30°, number of averages (number of excitations [NEX]) =1, echo train length (ETL) =1, pixel bandwidth (pBW) =250 Hz/pixel, field of view (FOV) =280 mm × 280 mm, matrix size = 96 × 96, acquisition time/slice = 3 s, and varied slice thickness. Evaluation of lesion formation involved T2-weighted (T2-W) turbo spin echo (TSE) imaging and visual inspection of the formed lesions by tissue dissection, which allowed measuring the real lesion dimensions. Notably,

Figure 2: Experimental setup for grid ablation in tissue-mimicking phantom/porcine tissue sample arranged on the table of a 3T magnetic resonance imaging scanner, with the key components indicated

FLASH sequences are characterized by rapid data acquisition, making them suitable for real-time applications such as the intraprocedural monitoring of temperature changes during FUS sonication, and have seen extensive use in numerous studies within the field.[39,43]

Effect of fast low-angle shot sequence parameters on motion accuracy

During these experiments, the device exhibited systematic motion errors, which were evident by the shifting of the sonicated points from the intended locations. Given the high intrinsic motion accuracy of the positioning mechanism[44] and the already established reliability of the MRgFUS system in precisely sonicating Regions of Interest (ROIs) of any shape,[44] the observed shifting was assumed to be caused by EMI between the time-varying magnetic fields of the scanner and mechatronic components. Therefore, the imaging parameters of the thermometry sequence were altered to assess their potential effect on the motion accuracy and observed lesion-shifting effects.

RESULTS

Figure 3 presents an indicative example of phantom sonication in a square grid pattern (8 × 8 with 5-mm step) with clear evidence of inaccurate ultrasonic delivery. The various sonication points were visited in a sequential manner, starting from the bottom right point and following an inter-row zig-zag motion, as shown in Figure 3a. Each point was sonicated using an acoustic power of 75 W and a sonication time of 30 s, leaving a 60-s delay between consecutive sonications, resulting in a maximum focal temperature of about 76°C (baseline temperature of 19°C). Figures 3b and c show coronal thermal dose maps following sonication of the 1st and final grid point, respectively. The focal temperature evolution recorded at the various sonication points within the phantom is shown in Figure 3d. Note in Figure 3c that as the grid progressed from the bottom to the top row the sonicated points were gradually

shifted towards the left direction, resulting in the ablation of a parallelogram-shaped area instead of a rectangular one. Note also that the thermal dose distribution of Figure 3c agrees well with the simulated necrosis region of Figure 3e.

The corresponding results for a similar grid sonication in freshly excised porcine tissue are shown in Figure 4. The planned sonication patern can be seen in Figure 4a. The shifting of lesions was initially evident by thermal mapping [Figure 4b] and then confirmed by follow-up T2-W imaging [Figure 4c] and visual inspection of the formed lesions on the dissected tissue [Figure 4d], providing clear evidence of systematic motion errors. In that case, the maximum focal temperature recorded was close to 70°C. The thermal map of Figure 4b reveals an average offset error between the actually sonicated spots and intended sonication points of about 4 mm. Note that in both cases [Figures 3 and 4] intraprocedural FLASH images were acquired with a slice thickness of 3 mm.

The effect of the selected slice thickness of the FLASH thermometry sequence on the shifting of sonicated points is revealed in Figures 5 and 6. In both cases, phantom sonications were performed in a 2 × 8 grid pattern with a 5-mm step. Figure 5 shows the thermal dose maps of the first and last (16th) sonications as extracted from FLASH images of different slice thicknesses of 3 mm, 6 mm, and 10 mm, being overlaid on a FLASH image of the phantom. Note that when the 3-mm slice was used, the two heated spots (corresponding to the 1st and 16th grid points) were about 4 mm apart (in the horizontal direction), whereas for the 6 mm and 10 mm slices, they were perfectly aligned, indicating excellent motion accuracy and repeatability. Figure 6 displays a series of postsonication T2-W TSE coronal images of the phantom, where the actual sonicated points appear as regions of increased intensity with excellent contrast from the background. In each case, intraprocedural FLASH imaging was performed using different slice thicknesses. These images reveal inaccurate ultrasonic delivery, except in the case of increasing the slice thickness to 8 mm.
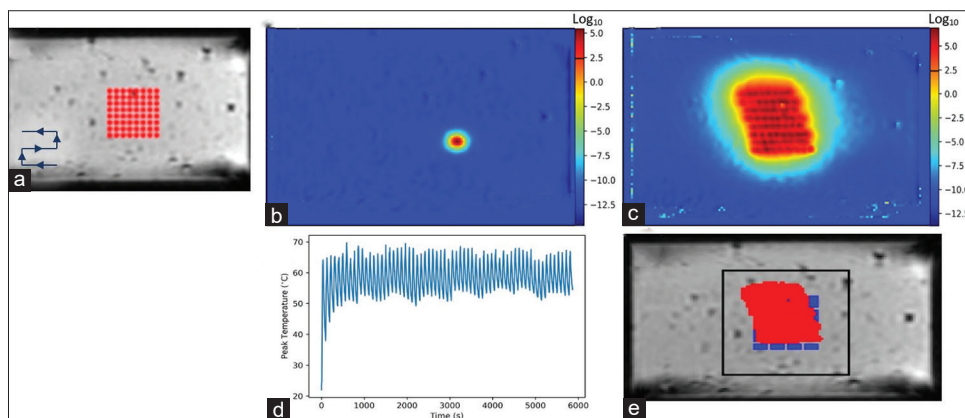

Figure 3: (a) Planned sonication pattern (8 × 8 with 5 mm step, 75 W acoustic power, 30 s on-time, 60 s cooling time), (b) Coronal thermal dose map extracted from fast low-angle shot (FLASH) images with slice thickness of 3 mm following sonication of the 1st point in the phantom. The black bar indicates a thermal dose of 240 CEM43°C, (c) Corresponding coronal thermal dose map following completion of the sonication grid, (d) Time series graph of the focal temperature evolution at the various sonication points within the phantom, (e) Necrosis map overlaid on FLASH magnitude image of the phantom
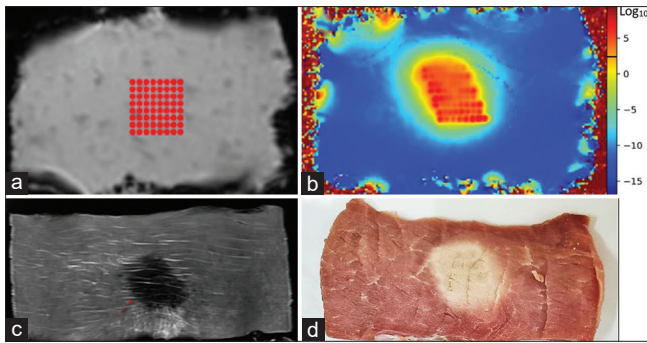
Figure 4: (a) Planned sonication pattern (8 × 8 with 5 mm step, 75 W acoustic power, 30 s on-time, 60 s cooling time), (b) Coronal thermal dose map extracted from FLASH images with slice thickness of 3 mm, following completion of the sonication grid in porcine tissue. The black bar indicates a thermal dose of 240 CEM43°C, (c) Coronal T2-weighted turbo spin echo image of tissue (repetition time = 4930 ms, echo time = 86 ms, flip angle = 110°, number of excitations = 2, pixel bandwidth = 250 Hz/pixel, field of view = 280 mm × 280 mm, matrix size = 256 × 256, slice thickness = 3 mm, and echo train length = 30) showing the inflicted overlapping lesions (red arrow), (d) Photo of tissue sliced horizontally at 20 mm revealing the overlapping lesions formed on a plane perpendicular to the beam

Based on these findings, the experiments were repeated using slice thicknesses of at least 6 mm for FLASH imaging. Figures 7 and 8 show representative outcomes of lesion formation in 8 × 8 and 4 × 4 grid patterns, respectively, demonstrating no shifting effects. In the former case, an acoustic power of 90 W was applied for 30 s to the various spots within the agar phantom, using a spatial step of 5 mm and a 60-s cooling period, resulting in the creation of an overlapping lesion in the desired rectangular shape. In the second case, identical acoustic parameters but a bigger spatial step of 15 mm were employed for sonicating a piece of freshly excised porcine tissue, resulting in the 16 equally spaced discrete lesions, as shown in Figure 8a. The thermal dose map of Figure 8b reveals well-defined spots, with accumulated thermal dose above the necrosis threshold being arranged in the planned pattern. The sonicated points were also visualized as spots of reduced intensity on postsonication T2-W images [Figure 8c]. Successful lesion formation was finally verified by visual inspection of the formed lesions on the dissected tissue [Figure 8d]. Note that a higher heat accumulation occurred in the first two sonication rows, resulting in the formation of bigger lesions.

DISCUSSION

The current study provides insights on the challenges of safely integrating a preclinical MRgFUS robotic system in a high-field MRI scanner in terms of motion accuracy using a series of sonications in TMPs and freshly excised porcine tissue. The thermal dose distribution was successfully monitored intraprocedurally using FLASH-based MR thermometry. However, the employed imaging sequence was proven to have a negative impact on the accuracy of motion and ultrasonic delivery
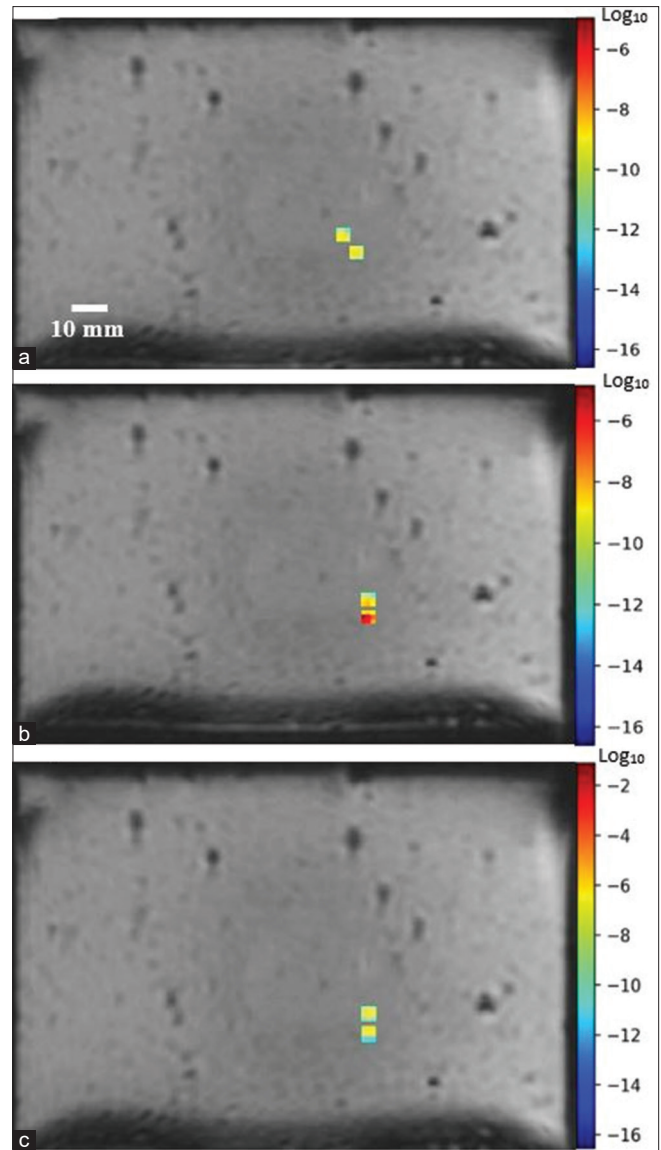

Figure 5: Thermal dose maps of the 1st and 16th points of a 2 × 8 sonication grid within the phantom (5-mm step, 90 W acoustic power, 5 s on-time, 5 s cooling time) as extracted from coronal FLASH images of the agar phantom using a slice thickness of. (a) 3 mm, (b) 6 mm, (c) 10 mm, being overlaid on a fast low-angle shot image of the phantom

since strong shifting of the heated spots and resultant lesions from the intended sonication points was observed. It was determined that these shifting effects could be prevented by proper selection of the imaging parameters employed for thermometry.

The offset errors between intended and actual transducer locations occurred in a systematic fashion, suggesting the presence of a systemic error in the device's operation during imaging. Random electromagnetic fluctuations can be naturally introduced in the MRI room from internal or external RF interference potentially affecting the system's operation. Except for EMI-induced errors, there are a number of other error sources that may influence the inherent motion accuracy of the system's positioning mechanism, which is about
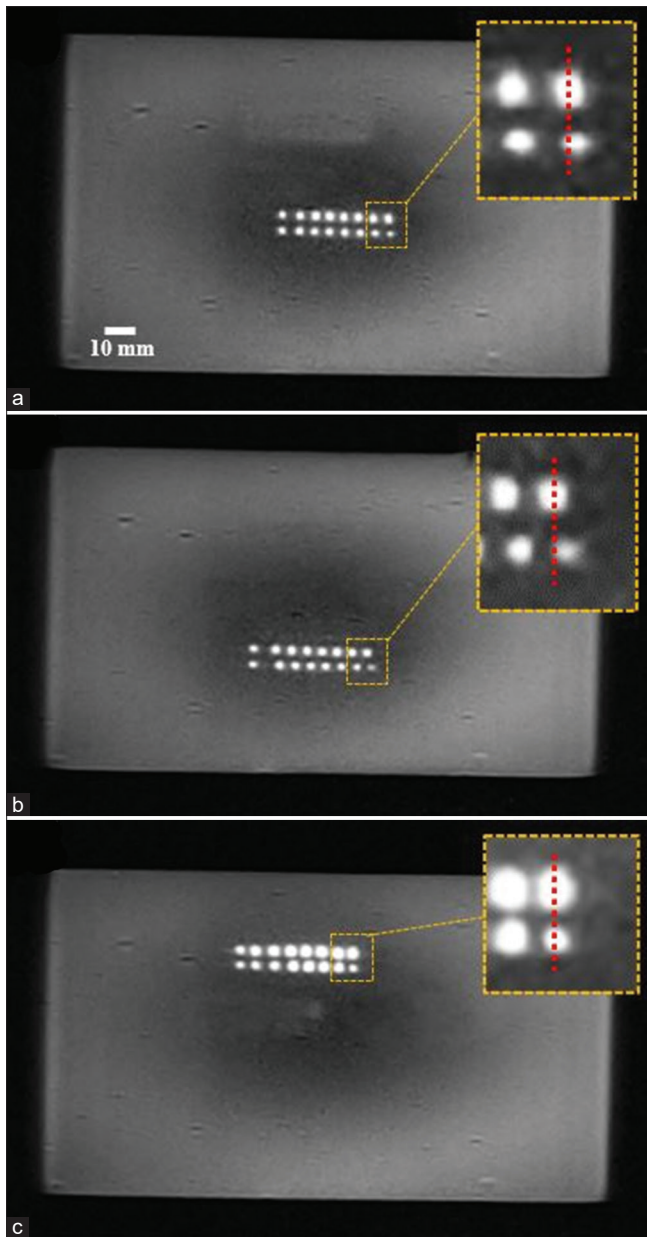
Figure 6: Coronal T2-weighted turbo spin echo images of the phantom (repetition time = 3000 ms, echo time = 52 ms, flip angle = 110°, number of excitations = 2, pixel bandwidth = 250 Hz/Pixel, field of view = 260 mm × 260 mm, slice thickness = 3 mm, matrix = 256 × 256, and echo train length = 30) acquired after grid sonications (2 × 8 with 5-mm step, 90 W acoustic power, 30 s on-time, 60 s cooling time) under fast low-angle shot-based magnetic resonance-thermometry guidance using different slice thickness of (a) 4 mm, (b) 6 mm, and (c) 8 mm

0.1 mm.[44] For instance, the accuracy of transducer positioning may be compromised by software bugs, communication problems between hardware and software, as well as errorsin the image registration process during planning. However, such errors typically appear in a random manner. Furthermore, the software navigation algorithms of the current system were extensively tested in previous work and proven to function

properly,[44] while robust communication between hardware and software was also established. Therefore, it was concluded that these potential sources of error are not the cause of the observed lesion-shifting effects, also considering that such issues could not be addressed by simply changing the imaging parameters. Therefore, the positioning errors were attributed to encoders' malfunctions.

MRI is based on three types of fields: a robust static magnetic field, a pulsed gradient magnetic field, and a pulsed RF field, which can potentially harm the function of motion-sensing electronics in robotic devices, thus compromising their reliability. The static magnetic field does not constitute a concern as far as ferrous materials are excluded from the design of sensing electronics. Optical encoders, such as those employed in the current MRgFUS system (EM10-500-I), are typically found in robotics and are generally considered MRI-compatible. In a previous study,[12] it was found that during image acquisition, deactivation of the encoders' counting pulses of an MRgFUS robot was crucial to preserving the imaging quality. In fact, deactivating the pulsing system led to an approximate 70% increase in the acquired SNR compared to having the counting pulses activated. The current study further demonstrates that during imaging, activated encoders can receive significant EMI signal leading to invalid position feedback, thereby compromising the accuracy of ultrasonic delivery. Contrary to the current findings, there are few studies reporting that optical encoders performed properly in 3T scanners, without any evidence of missed counts.[17-20] In most of these studies, T1-W and T2-W sequences with a small slice thickness of 3 mm were employed for MR compatibility evaluation.[18,20] Therefore, since different scanning parameters were used, a direct comparison with the present study is not practicable.

Increasing the slice thickness of the thermometry sequence (FLASH) was proven an efficient method to minimize the effect of imaging on the encoders' counting and preserve the accuracy of treatment delivery. The use of a slice thickness smaller than 6 mm showed bad performance in terms of robotic motion accuracy, as the sonicated points were systematically shifted from the intended locations with an error close to 4 mm. It seems that in these cases, a strong EMI was detected and wrongly interpreted as motion by the encoders, thus leading to wrong motion decision. The slice thickness of 6 mm yielded uncertain outcomes since shifting effects were detected in a few cases. On the contrary, accurate delivery of ultrasonic energy to the desired locations was consistently observed when employing slice thicknesses of at least 8 mm, demonstrating high accuracy and repeatability of motion and negligible noise accumulation by the encoder. Considering the multitude of factors influencing EMI between the scanner and electronic devices and the intricate connection between imaging parameters and the distribution of RF fields, the exact reason for this observation remains unclear. Further research is warranted to examine this thoroughly and is considered for future study. It should also be made clear that these quantitative
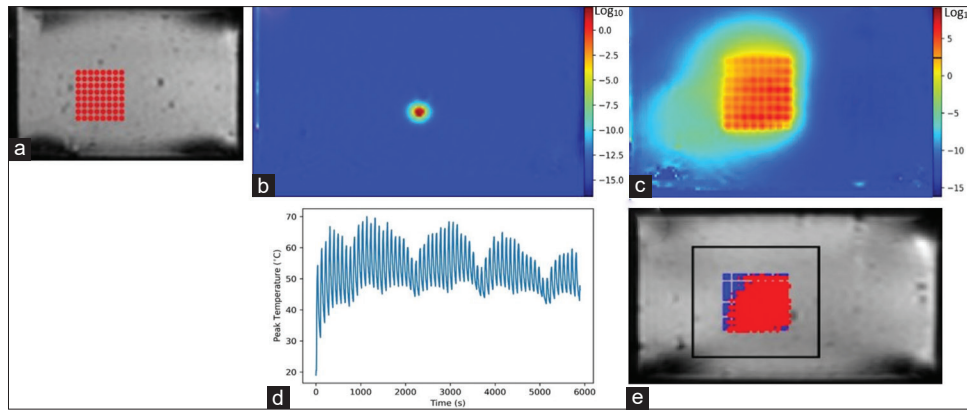
Figure 7: (a) Planned sonication pattern (8 × 8 with 5 mm step, 90 W acoustic power, 30 s on-time, 60-s cooling time), (b) Coronal thermal dose map extracted from fast low-angle shot (FLASH) images with slice thickness of 6 mm, following sonication of the 1st point in the phantom. The black bar indicates a thermal dose of 240 CEM43°C, (c) Corresponding thermal dose map following completion of the sonication grid, (d) Time series graph of the focal temperature evolution at the various sonication points within the phantom, (e) Necrosis map overlaid on FLASH image of the phantom
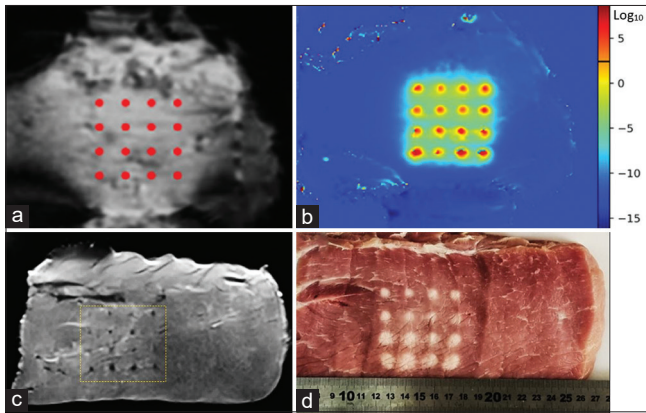

Figure 8: (a) Planned sonication pattern (4 × 4 with 15 mm step, 75 W acoustic power, 30 s on-time, 60 s cooling time), (b) Coronal thermal dose map extracted from fast low-angle shot images with slice thickness of 10 mm, following completion of the sonication grid in porcine tissue. The black bar indicates a thermal dose of 240 CEM43°C, (c) Postsonication coronal T2-weighted turbo spin echo image (repetition time = 2500 ms, echo time = 55 ms, flip angle = 110°, number of excitations = 2, pixel bandwidth = 219 Hz/pixel, field of view = 260 mm × 260 mm, matrix size = 128 × 128, slice thickness = 3 mm, and echo train length = 12) of tissue acquired with deep resolve reconstruction, showing the inflicted discrete lesions (yellow square), (d) Photo of tissue sliced horizontally at 20 mm showing the discrete lesions formed on a plane perpendicular to the beam

results specifically apply to the positioning system employed in the study and may vary when considering other systems, protocols, or methodologies.

Other studies reporting errors in encoders' operation in the MRI setting proposed saving and restoring preimaging encoder counts, as well as deactivating the encoder feedback during image acquisition to address this issue. However, this is not practical in the context of MRgFUS since it will prolong the procedure time significantly. Simultaneous imaging and robotic motion are required to maintain an efficient procedural workflow in the case of MRgFUS

ablation in grid patterns. The current study suggests a more straightforward measure to correct this by simply increasing the slice thickness. Nevertheless, this comes at the cost of less precise temperature measurements, which becomes more apparent in the case of sharp spatial temperature fluctuations. Specifically, given that the temperature changes occurring across the entire slice are averaged out, the spatial resolution of thermometry measurements is unavoidably reduced. Therefore, it is suggested that the choice of slice thickness should be a balance between the spatial resolution of thermometry and EMI-induced motion errors. The herein findings suggest using at least an 8-mm thickness to ensure accurate positioning of the ultrasonic source and sonication of the targeted locations. It should be though emphasized that this conclusion applies to the specific MRgFUS system and imaging sequences employed in the study and may differ among systems.

To the best of our knowledge, no data have been previously reported on the correlation between MR imaging parameters and the operation of robotic devices within an MRI scanner regarding the motion accuracy and reliability of ultrasonic delivery. There is literature reporting that malfunctioning of implantable cardiac devices can be prevented by adjusting the imaging parameters, such as by increasing the slice thickness or reducing the receiver bandwidth.[45] Furthermore, in the study of Shokrollahi *et al.*,[46] who explored the challenges of incorporating ultrasonic motors in the MRI environment, reduction of the slice thickness and increase of the bandwidth were proposed as simple methods for mitigating susceptibility artifacts introduced in the images. In fact, a significant reduction in the artifact size of up to 75% occurred by reducing the slice thickness from 5 to 1 mm. However, the authors did not investigate the direct effect on the motors' operation.

Evaluation of the motion accuracy of MR-compatible FUS robots usually involves MRI-based methods, where TMPs[47,48] and *ex vivo* animal tissue[49] are sonicated in simple grid patterns. The motion accuracy is commonly assessed by superimposing thermal images[47] or TSE images[48,49] acquired

after each sonication to assess the spacing between heated regions or formed lesions, respectively. Since imaging is not performed during positioning of the ultrasonic source, EMI-induced errors in robotic motion are less likely to be detected. It seems that a more comprehensive investigation should be performed to safely conclude the accurate motion of MRgFUS devices in the MRI environment, provided that continuous imaging is essential for efficient thermal mapping and monitoring of the FUS-induced tissue effects. Optimization of the thermometry sequence parameters to avoid EMI-induced errors in the sensing electronics may be required to meet the clinical requirements for safety.

The discussion should also address the occasional variation in lesion size observed following grid sonications in excised porcine tissue [Figure 8]. Due to its physiological and anatomical similarities to human tissue, porcine tissue is commonly used in preclinical research. However, it is typically characterized by irregularities in tissue surface and variability in tissue composition, such as the presence of fat layers, which can lead to scattering and phase aberrations. In addition, the presence of air bubbles within the tissue may result in strong acoustic reflections. These factors affect the propagation and penetration depth of ultrasonic waves, further influencing the formation of uniform lesions in tissue.

CONCLUSIONS

In the course of evaluating an MRgFUS preclinical robotic system, the current study yielded some interesting findings. Strong shifting of the heated spots from the planned locations occurred during MR-thermometry-guided grid sonications in TMPs and *ex vivo* porcine tissue. It was determined that this phenomenon originates from EMI-induced malfunctions in the encoders' operation and depends on the selected slice thickness of the thermometry sequence. Increasing the slice thickness was found effective in correcting the observed shifting effects, but it should be done keeping in mind the potential negative effects on the accuracy and spatial resolution of thermometry. Overall, these findings raise awareness about EMI effects on the motion accuracy of robotic devices in the context of MRgFUS but also in the wider field of MR-guided robotics and propose the proper selection of imaging parameters as a simple measure to mitigate these effects.

Financial support and sponsorship

Conflicts of interest

There are no conflicts of interest.

REFERENCES

1. Su H, Kwok KW, Cleary K, Iordachita I, Cavusoglu MC, Desai JP, *et al.* State of the art and future opportunities in MRI-guided robot-assisted surgery and interventions. Proc IEEE Inst Electr Electron Eng 2022;110:968-92.
2. Farooq MU, Ko SY. A decade of MRI compatible robots: Systematic review. IEEE Trans Robot 2023;39:862-84.
3. Su H, Iordachita II, Tokuda J, Hata N, Liu X, Seifabadi R, *et al.* Fiber optic force sensors for MRI-guided interventions and rehabilitation: A review. IEEE Sens J 2017;17:1952-63.
4. Chinzei K, Kikinis R, Jolesz FA. MR Compatibility of Mechatronic Devices: Design Criteria. In: Proceedings of the Second International Conference on Medical Image Computing and Computer-Assisted Intervention; 2006. p. 1020-30.
5. Huang S, Gao A, Wu Z, Lou C, Wang Y, Yang GZ. An MR safe rotary encoder based on eccentric sheave and FBG sensors. Proc IEEE Int Conf Robot Autom 2021;2021:9410-6.
6. Krieger A, Song SE, Cho NB, Iordachita I, Guion P, Fichtinger G, *et al.* Development and evaluation of an actuated MRI-compatible robotic system for MRI-guided prostate intervention. IEEE ASME Trans Mechatron 2012;18:273-84.
7. Fischer GS, Krieger A, Iordachita I, Csoma C, Whitcomb LL, Gabor F. MRI compatibility of robot actuation techniques – A comparative study. Med Image Comput Comput Assist Interv 2008;11:509-17.
8. Yiannakou M, Menikou G, Yiallouras C, Ioannides C, Damianou C. MRI guided focused ultrasound robotic system for animal experiments. Int J Med Robot 2017;13:e1804. [doi: 10.1002/rcs. 1804].
9. Damianou C, Giannakou M, Menikou G, Ioannou L. Magnetic resonance imaging-guided focused ultrasound robotic system with the subject placed in the prone position. Digit Med 2020;6:24-31.
10. Antoniou A, Giannakou M, Evripidou N, Stratis S, Pichardo S, Damianou C. Robotic system for top to bottom MRgFUS therapy of multiple cancer types. Int J Med Robot 2022;18:e2364.
11. Giannakou M, Antoniou A, Damianou C. Preclinical robotic device for magnetic resonance imaging guided focussed ultrasound. Int J Med Robot 2023;19:e2466.
12. Antoniou A, Georgiou L, Evripidou N, Ioannides C, Damianou C. Challenges regarding MR compatibility of an MRgFUS robotic system. J Magn Reson 2022;344:107317.
13. Goldenberg AA, Trachtenberg J, Kucharczyk W, Yi Y, Haider M, Ma L, *et al.* Robotic system for closed-bore MRI-guided prostatic interventions. IEEE/ASME Trans Mechatron 2008;13:374-9.
14. Elhawary H, Tse ZT, Hamed A, Rea M, Davies BL, Lamperth MU. The case for MR-compatible robotics: A review of the state of the art. Int J Med Robot 2008;4:105-13.
15. Knull E, Bax JS, Park CK, Tessier D, Fenster A. Design and validation of an MRI-compatible mechatronic system for needle delivery to localized prostate cancer. Med Phys 2021;48:5283-99.
16. Yang B, Roys S, Tan UX, Philip M, Richard H, Gullapalli R, *et al.* Design, development, and evaluation of a master-slave surgical system for breast biopsy under continuous MRI. Int J Rob Res 2014;33:616-30.
17. Su H, Harrington K, Cole G, Wang Y, Fischer GS. Modular Needle Steering Driver for MRI-Guided Transperineal Prostate Intervention. IEEE International Conference on Robotics and Automation Work Snakes, Worms Catheter Continuum and Serpentine Robots for Minimally Invasive Surgery; 2010. p. 2-5.
18. Fischer GS, Iordachita I, Csoma C, Tokuda J, Dimaio SP, Tempany CM, *et al.* MR-compatible pneumatic robot for transperineal prostate needle placement. IEEE ASME Trans Mechatron 2008;13:295-305.
19. Cepek J, Chronik BA, Lindner U, Trachtenberg J, Davidson SR, Bax J, *et al.* A system for MRI-guided transperineal delivery of needles to the prostate for focal therapy. Med Phys 2013;40:012304.
20. Li G, Su H, Cole GA, Shang W, Harrington K, Camilo A, *et al.* Robotic system for MRI-guided stereotactic neurosurgery. IEEE Trans Biomed Eng 2015;62:1077-88.
21. Wendt O, Oellinger J, Lüth TC, Felix R, Boenick U. The effects of the use of piezoelectric motors in a 1.5-tesla high-field magnetic resonance imaging system (MRI). Biomed Tech (Berl) 2000;45:20-5.
22. Chopra R, Baker N, Choy V, Boyes A, Tang K, Bradwell D, *et al.*

MRI-compatible transurethral ultrasound system for the treatment of localized prostate cancer using rotational control. Med Phys 2008;35:1346-57.

23. Gunderman A, Montayre R, Ranjan A, Chen Y. Review of robot-assisted HIFU therapy. Sensors (Basel) 2023;23:3707.

24. Yiallouras C, Damianou C. Review of MRI positioning devices for guiding focused ultrasound systems. Int J Med Robot 2015;11:247-55.

25. Epaminonda E, Drakos T, Kalogirou C, Theodoulou M, Yiallouras C, Damianou C. MRI guided focused ultrasound robotic system for the treatment of gynaecological tumors. Int J Med Robot 2016;12:46-52.

26. Menikou G, Yiallouras C, Yiannakou M, Damianou C. MRI-guided focused ultrasound robotic system for the treatment of bone cancer. Int J Med Robot 2017;13. [doi: 10.1002/rcs. 1753].

27. Antoniou A, Giannakou M, Evripidou N, Evripidou G, Spanoudes K, Menikou G, *et al.* Robotic system for magnetic resonance guided focused ultrasound ablation of abdominal cancer. Int J Med Robot 2021;17:e2299.

28. Drakos T, Giannakou M, Menikou G, Filippou A, Evripidou N, Spanoudes K, *et al.* MRI-guided focused ultrasound robotic system for preclinical use. J Vet Med Anim Sci 2021;4:1-11.

29. Giannakou M, Drakos T, Menikou G, Evripidou N, Filippou A, Spanoudes K, *et al.* Magnetic resonance image-guided focused ultrasound robotic system for transrectal prostate cancer therapy. Int J Med Robot 2021;17:e2237.

30. Filippou A, Evripidou N, Damianou C. Robotic system for magnetic resonance imaging-guided focused ultrasound treatment of thyroid nodules. Int J Med Robot 2023;19:e2525.

31. Drakos T, Giannakou M, Menikou G, Constantinides G, Damianou C. Characterization of a soft tissue-mimicking agar/wood powder material for MRgFUS applications. Ultrasonics 2021;113:106357.

32. Drakos T, Antoniou A, Evripidou N, Alecou T, Giannakou M, Menikou G, *et al.* Ultrasonic attenuation of an Agar, Silicon Dioxide, and evaporated milk gel phantom. J Med Ultrasound 2021;29:239-49.

33. Antoniou A, Georgiou L, Christodoulou T, Panayiotou N, Ioannides C, Zamboglou N, *et al.* MR relaxation times of agar-based tissue-mimicking phantoms. J Appl Clin Med Phys 2022;23:e13533.

34. Rieke V, Butts Pauly K. MR thermometry. J Magn Reson Imaging 2008;27:376-90.

35. Bing C, Staruch RM, Tillander M, Köhler MO, Mougenot C, Ylihautala M, *et al.* Drift correction for accurate PRF-shift MR thermometry during mild hyperthermia treatments with MR-HIFU. Int J Hyperthermia 2016;32:673-87.

36. Mougenot C, Moonen C. Magnetic resonance-guided high intensity focused ultrasound in the presence of biopsy markers. J Ther Ultrasound 2017;5:25.

37. Antoniou A, Evripidou N, Georgiou L, Chrysanthou A, Ioannides C, Damianou C. Tumor phantom model for MRI-guided focused ultrasound ablation studies. Med Phys 2023;50:5956-68.

38. Partanen A, Yarmolenko PS, Viitala A, Appanaboyina S, Haemmerich D, Ranjan A, *et al.* Mild hyperthermia with magnetic resonance-guided high-intensity focused ultrasound for applications in drug delivery. Int J Hyperthermia 2012;28:320-36.

39. Antoniou A, Evripidou N, Damianou C. Focused ultrasound heating in brain tissue/skull phantoms with 1 MHz single-element transducer. J Ultrasound 2023. [doi: 10.1007/s40477-023-00810-7].

40. Dewhirst MW, Viglianti BL, Lora-Michiels M, Hanson M, Hoopes PJ. Basic principles of thermal dosimetry and thermal thresholds for tissue damage from hyperthermia. Int J Hyperthermia 2003;19:267-94.

41. Yarmolenko PS, Moon EJ, Landon C, Manzoor A, Hochman DW, Viglianti BL, *et al.* Thresholds for thermal damage to normal tissues: An update. Int J Hyperthermia 2011;27:320-43.

42. Sapareto SA, Dewey WC. Thermal dose determination in cancer therapy. Int J Radiat Oncol Biol Phys 1984;10:787-800.

43. Evripidou N, Antoniou A, Georgiou L, Ioannides C, Spanoudes K, Damianou C. MRI compatibility testing of commercial high intensity focused ultrasound transducers. Phys Med 2024;117:103194.

44. Antoniou A, Drakos T, Giannakou M, Evripidou N, Georgiou L, Christodoulou T, *et al.* Simple methods to test the accuracy of MRgFUS robotic systems. Int J Med Robot 2021;17:e2287.

45. Götte MJ, Rüssel IK, de Roest GJ, Germans T, Veldkamp RF, Knaapen P, *et al.* Magnetic resonance imaging, pacemakers and implantable cardioverter-defibrillators: Current situation and clinical perspective. Neth Heart J 2010;18:31-7.

46. Shokrollahi P, Drake JM, Goldenberg AA. A study on observed ultrasonic motor-induced magnetic resonance imaging (MRI) artifacts. Biomed J 2019;42:116-23.

47. Price KD, Sin VW, Mougenot C, Pichardo S, Looi T, Waspe AC, *et al.* Design and validation of an MR-conditional robot for transcranial focused ultrasound surgery in infants. Med Phys 2016;43:4983.

48. Yiallouras C, Ioannides K, Dadakova T, Pavlina M, Bock M, Damianou C. Three-axis MR-conditional robot for high-intensity focused ultrasound for treating prostate diseases transrectally. J Ther Ultrasound 2015;3:2.

49. Mylonas N, Damianou C. MR compatible positioning device for guiding a focused ultrasound system for the treatment of brain deseases. Int J Med Robot 2014;10:1-10.